

Effect of the boron content on the amorphisation process and magnetic properties of the mechanically alloyed $\text{Fe}_{92-x}\text{Nb}_8\text{B}_x$ powders

T. Chabi¹, N. Bensebaa¹, S. Alleg^{1,*}, S. Azzaza¹, J.J. Suñol², E.K. Hlil³

¹Laboratoire de magnétisme et Spectroscopie des Solides (LM2S), Département de Physique, Université Badji Mokhtar Annaba, BP 12, 23000 Annaba, Algeria.

²Dept. De Fisica, Universitat de Girona, Campus Montilivi, 17071 Girona, Spain.

³Institut NEEL, CNRS, Université Grenoble Alpes, 25 Rue des Martyrs BP 166
38042 Grenoble cedex 9, France.

* Corresponding author e-mail address: safia.alleg@univ-annaba.dz

Tel/fax: +213 774312482

Abstract:

The effect of the B content on the microstructural, structural and magnetic properties of partially amorphous $\text{Fe}_{92-x}\text{Nb}_8\text{B}_x$ ($x = 5, 10, 15$ and 20) alloys have been investigated by means of scanning electron microscopy, X-ray diffraction, BS1 and BS2 magnetometers. The XRD results reveal the formation of a nanocomposite structure where nanocrystalline bcc α -Fe and Fe_2B phases are embedded into an amorphous matrix. The FeB boride is observed for higher boron contents ($x=15$ and 20) and the crystallite sizes are in the range of 7-24 nm. As the B content increases, the amorphous relative proportion and coercivity increase, whereas the saturation magnetization decreases. An important magnetic hardening occurs by lowering the temperature from 400 to 5 K for $x=20\%$ B. The variation of the Curie temperature can be attributed to the heterogeneity of the amorphous matrix.

Keywords: Nanocrystalline materials; Mechanical alloying; Fe-Nb-B alloys; X-ray diffraction; Magnetic properties.

1. Introduction

Mechanical alloying (MA) or high energy ball milling (HEBM) is one of the various techniques used to synthesize nanocrystalline (NC) materials. It is a powder metallurgy method where the starting elemental or prealloyed powders are subjected to a high-speed deformation mechanism (10^3 to 10^{-3} s⁻¹) by heavy plastic deformation, fracture, cold welding, rewelding and agglomeration. The final product is achieved by controlling several parameters which are related to each other such as the ball mill type, milling time, milling temperature, ball to-powder weight ratio (BPR), rotation speed, process control agent, grinding media (balls, material, volume of the vial...), and milling atmosphere. HEBM has proved its suitability and availability as one of the powerful and simple techniques for producing amorphous alloys, nanostructured materials, solid solutions and intermetallics [1–10].

The FeMB alloys (M= Zr, Hf, Nb) or Nanoperm, which contain around 80% of iron, 7% of transition metals (Zr, Hf, Nb) and 13% of boron, are structurally and magnetically biphasic since they are composed of hard ferromagnetic nanograins dispersed homogeneously into a soft ferromagnetic amorphous matrix [11]. These materials are very interesting due to their soft magnetic properties such as effective permeability and saturation magnetic flux density [12–15]. Consequently, they can be used in many industrial applications such as telecommunications, power electronics, micro-devices, generators and sensors. The augmentation of both B and Nb percentages in the Fe-based amorphous alloys play a main role in the thermal stability [10]. The outcome is that the nanocrystallization takes place in the form of pure iron crystals which favor a high saturation induction (1.5–1.7 T) and a Curie temperature, T_c, close to 769°C. Furthermore, Nanoperm alloys lose their magnetization with the formation of borides [16]. Among the nanoperm, the ternary Fe-Nb-B system has attracted much attention owing to its useful properties [17–19], and has been prepared in ribbons form by melt spinning [20] and planar flow casting [21], bulk form by arc melting [15] and powder form by MA [18]. Depending on the B content, it has been reported that the end product consists, generally, of a mixture of bcc α -Fe, borides and amorphous phases [22]. In the ball milled Fe_{94-x}Nb₆B_x (x = 9, 14, 20) alloys, it has been found that the Fe lattice parameter increases with increasing B content while the crystallite size decreases [23] and the boron atoms segregate at the grain boundaries [7]. The Fe_{65+x}Nb₁₀B_{25-x} (x = 0,5, 10) metallic glasses prepared by arc melting exhibit soft magnetic properties in the glassy state and their nanocrystallization leads to the enhancement of the coercivity [24]. A mixture of α -Fe, Nb(B)

1 and highly disordered Fe(Nb, B) solid solution has been obtained in the mechanically alloyed
2 Fe₆₂Nb₈B₃₀ powders for 25 h, while the paramagnetic amorphous structure is achieved on
3 further milling time [18]. It is obvious that the preparation conditions influence the end
4 product and the properties of the mechanically alloyed powders. Consequently, the aim of the
5 present work is to study the effect of boron content on the amorphisation process, structural,
6 microstructural, morphological and magnetic properties of the ball milled Fe_{92-x}Nb₈B_x (x = 5,
7 10, 15 and 20) powders. An accurate quantitative phase analysis (QPA) was used to determine
8 the amorphous phase relative proportion by using the MAUD program [25].
9
10
11
12
13
14
15

16 2. Experimental details

17 Fe_{92-x}Nb₈B_x (x= 5, 10, 15 and 20) powder mixtures were mechanically alloyed for 50 h
18 from pure elemental powders of Fe (6-8 μm, 99.7%), Nb (74 μm, 99.85%) and amorphous B
19 (>99%). The milling process was performed in a planetary ball mill Retsch PM400 under an
20 argon atmosphere using hardened steel vials and balls. The ball-to-powder weight ratio was
21 about 7:1 and the rotation speed was 700 rpm. In order to avoid the excessive increase of the
22 temperature inside the vials, the milling process was interrupted each 1/2 h for 1/4 h.
23 Morphological changes of the powder particles were followed by scanning electron
24 microscopy (SEM) in DSM960A Zeiss apparatus equipped with energy dispersive X-ray
25 spectroscopy (EDX). The structural evolution was investigated by X-ray diffraction (XRD) by
26 means of PANalytical Empyrean diffractometer in a (θ - θ) Bragg Brentano geometry with
27 Co-K α radiation (λ_{Co} =1.78901 Å). Phase identification, lattice parameters (a, c), average
28 crystallite size, $\langle L \rangle$, root-mean square (r.m.s) strains, $\langle \sigma^2 \rangle^{1/2}$, phases relative proportion,
29 atomic positions, etc. were obtained from the refinement of the XRD patterns by the MAUD
30 program which is based on the Rietveld method [26] combined with Fourier analysis which is
31 well adapted for disordered alloys. The saturation magnetization, coercivity, saturation to
32 remanence ratio and Curie temperatures were determined by measuring $M(H)$ hysteresis loops
33 and $M(T)$ curves using the BS1 and BS2 extraction-type magnetometers developed at Néel
34 Institute for high and low temperatures, respectively.
35
36
37
38
39
40
41
42
43
44
45
46
47
48
49
50

51 3. Results and discussion

52 3.1. Morphological evolution

1 The powder particles are subjected to flattening, fracturing, cold welding and rewelding
2 during the milling process. Consequently, the formed fresh surfaces show a high activity
3 which results in strong bonding between the hard phases and the metallic matrix. **Figure 1**
4 displays the morphological changes of the ball milled $\text{Fe}_{92-x}\text{Nb}_8\text{B}_x$ ($x= 5, 10, 15$ and 20)
5 powders for 50 h. One observes that the powder morphologies are different from each other.
6 The ductile particles are flattened by the compressive forces due to the collision of the balls
7 inside the vials, while the brittle particles (boron) are fractured and welded. Hence, the micro-
8 forging process causes a change in the shape of the individual particles. The existence of
9 bigger and small particles results from the competition between fracturing and cold welding.
10 For 20% B, the important microstructural refinement can be related to the domination of the
11 fracturing process since the boron element is hard and brittle. The EDX analysis shows that
12 each particle contains the initial Fe, Nb and B elements (**Table 1**). The elemental composition
13 fluctuation might be due to the heterogeneity of the powder particles.
14
15
16
17
18
19
20
21
22
23

24 **3.2. Phase formation**

25 **Figure 2** illustrates the evolution of the XRD patterns of the $\text{Fe}_{92-x}\text{Nb}_8\text{B}_x$ alloys as a
26 function of B content. The widening of the diffraction peaks and the reduction of their
27 intensities are related to the decrease of the crystallite size and the increase of the internal
28 level strains. In addition to the broad amorphous halo (located at about $2\theta=52^\circ$), sharp
29 diffraction peaks linked to NC α -Fe and Fe_2B phases are observed. For 15%B and 20%B
30 samples, one notes also the appearance of new diffraction peaks related to the formation of
31 the FeB boride. Accordingly, the Rietveld refinements of the XRD patterns were performed
32 by introducing either three or four phases among the following structures: bcc α -Fe (space
33 group $Im\bar{3}m$, lattice parameter $a_0=0.2866$ nm), tetragonal Fe_2B boride (space group $I4/mcm$,
34 lattice parameters $a_0=0.511$ nm and $c_0=0.4249$ nm), orthorhombic FeB (space group
35 $Pbnm:cab$, lattice parameters $a_0=0.4053$ nm, $b_0=0.5495$ nm and $c_0=0.2946$ nm) and
36 amorphous phase (**Fig. 3**). This later was quantified according to Le Bail model [25] by
37 keeping $\langle L \rangle = 10$ nm and $\langle \sigma^2 \rangle^{1/2} = 0.001$, while the lattice parameter is refined. The
38 obtained results are summarized in **Table 2**.
39
40
41
42
43
44
45
46
47
48
49
50
51

52 The presence of the metalloid B in the Fe–Nb–B alloys obstructs coarsening of the
53 bcc grains, enhances the glass forming ability (GFA), provides good magnetic properties and
54 gives a better thermal stability of the residual amorphous phase [27]. Moreover, the formation
55 of the amorphous phase in the mechanically alloyed Fe-Nb-B system can be related to the
56
57
58
59
60
61
62
63
64
65

1 important amount of structural defects and impurity atoms in the interstitial sites which
2 distorted locally the crystal lattice. Consequently, the interdiffusion between the elemental
3 powders is accelerated and the free energy of the crystalline phases is enlarged compared to
4 the free energy of the amorphous ones leading to an atomic disorder and facilitating the
5 amorphisation process. Furthermore, the packed local structure is favored by the segregation
6 of boron inclusions at the grain boundaries, the stronger attractive interaction between Fe and
7 B atoms as well as the presence of three elements (Fe, Nb and B) with significant difference
8 in atomic size ratios ($r_{\text{Nb}}=0.198 \text{ nm} > r_{\text{Fe}}=0.124 \text{ nm} > r_{\text{B}}=0.087 \text{ nm}$). When the local atomic
9 strains generated by size differences between B, Nb and Fe attain a critical level, the local
10 atomic coordination number changes and the topological instability of the crystalline lattice
11 leads to the formation of the amorphous phase. This later occurs at the Fe/B, Fe/Nb and Nb/B
12 interfaces and the mixing of the elemental powders at the atomic level is favored by the high
13 negative heats of mixing which are of about -26 kJ/mol , -16 kJ/mol and -54 kJ/mol for Fe-
14 B, Nb-Fe and Nb-B [28], respectively. Furthermore, the formation of the amorphous phase
15 can be accelerated by the increase of the boron content. Indeed, in the Fe-based alloys with
16 less than 12 at.% B a metastable bcc Fe(B) supersaturated solid solution was obtained instead
17 of an amorphous phase [18, 29].

18 The formation of Fe_2B and FeB iron borides can be attributed to the reaction between
19 Fe and B with similar diffusion coefficients [30] as well as the excess of boron content which
20 is introduced into the Fe matrix during the milling process, although its solubility is less than
21 0.02 wt.% at room temperature [31]. Besides, the diffusivity of solute elements into the iron
22 matrix might be enhanced by the presence of a variety of crystal defects (dislocations,
23 vacancies, stacking faults and grain boundaries) that are introduced by the heavy plastic
24 deformation into the powder particles. Consequently, the refined microstructural features
25 decrease the diffusion distances and the slight increase in temperature during the milling
26 process helps the diffusion process leading to the formation of intermetallic compounds.
27 According to the binary Fe-B phase diagram [31], Fe_2B and FeB boride phases can be formed
28 at the thermodynamic equilibrium with a B content of about 8.8 wt% and 16 wt%,
29 respectively.

30 The crystallite size of the obtained phases varies between 7 and 24.3 nm. One notes
31 that the α -Fe crystallite size increases as a function of B content (Table 2), while that of the
32 Fe_2B phase remains constant (Fig.4). The relative proportion of Fe_2B phase (Fig. 5) increases
33 to 38.9 % for 10 %B, decreases for 15%B and levels off. This decrease might be correlated to

1 the segregation of B atoms in the grain boundaries. Such particular behavior might be
2 ascribed to the instability of the segregation process and its effect can be inhibited beyond this
3 critical concentration. Similar comportment was observed in the $\text{Fe}_{60}\text{Al}_{40-x}\text{B}_x$ alloys [32].
4

5 The lattice parameter of α -Fe is B content independent (Fig. 6) while that of the highly
6 disordered amorphous type structure increases relatively. Such an increase might be due to its
7 enrichment by the Nb atoms. For the Fe_2B boride phase, the lattice parameters a and c exhibit
8 an antagonist behavior as a function of B content (Fig. 7). Indeed, the lattice parameter a
9 decreases linearly whereas c increases slightly up to 15%B and then rapidly for 20%B. The
10 relative deviations of the lattice parameters a and c are of about $\Delta a = -1\%$ and $\Delta c = 1.82\%$. The
11 lattice distortion which is characterized by lattice expansion and/or contraction can be
12 attributed to the presence of a great quantity of point defects or vacancies inside the
13 nanometer crystallites due to their higher energetic solution.
14
15
16
17
18
19
20
21
22
23

24 3.3. Magnetic properties

25 The hysteresis loops of the mechanically alloyed $\text{Fe}_{92-x}\text{Nb}_8\text{B}_x$ powders, $M(H)$, taken
26 at different temperatures, are displayed in Figure 8 as a function of boron content. The insets
27 show the enlargement of the low-field portion of the hysteresis loops as well as the first
28 magnetization curves. The magnetic properties are dependent on the sample microstructure
29 such as crystallite size, particle morphology, structural defects, etc. The hysteresis curves
30 display typical soft magnetic characteristics and the steep augmentation in $M(H)$ near
31 $\mu_0 H_a = 0$ can be due to domain-wall movement. Figure 9 reveals that the variation of
32 coercivity H_c as a function of B content exhibits the same trend as that of the amorphous
33 phase proportion. Indeed, H_c increases with the augmentation of B content. Furthermore, the
34 magnetic hardening at low temperatures is evidenced by the important increase of coercive
35 field for 20%B sample from 0.014 to 0.0595 T by lowering the temperature from 400 to 5 K,
36 respectively. The augmentation of H_c might be linked to the presence of small precipitates
37 within the hard magnetic phase. For example, boron is a brittle and hard material and
38 consequently, boron inclusions remain without mixing in the matrix even after mechanical
39 amorphization of the material. Also, the very small miscibility of Fe, Nb and B leads to the
40 presence of unmixed inclusions within the amorphous phase which impede the domain wall
41 movement leading to the increase of coercivity. Such an assumption can be confirmed by the
42 increase of the amorphous phase relative proportion as a function of B content.
43 Simultaneously, the saturation magnetization M_s decreases with increasing B content as
44
45
46
47
48
49
50
51
52
53
54
55
56
57
58
59
60

1 shown in Figure 10. The drop of M_s might be due to the formation of the hard magnetic phase
2 Fe_2B as well as to the structural disorder which is introduced during the milling process.
3 Consequently, the magnetic moment decreases through the change in the configuration of the
4 nearest neighbors of magnetic Fe atoms *via* the substitution of Fe atoms by Nb and/or B ones.
5 In fact, the magnetic atomic moment is assumed to depend on the number of magnetic and
6 metalloid atoms in the first nearest-neighbor shell. Therefore, the decrease of M_s can be
7 correlated to the decrease of the coordination of nearest-neighbor magnetic atoms due to the
8 high metalloid content at.% (Nb+B). Comparable results have been reported on the decrease
9 of M_s as the formation of the amorphous phase is accelerated [6]. The remanence to saturation
10 ratio, Mr/M_s , is plotted against B content for different temperatures in Figure 11. By
11 comparing the Mr/M_s values with those of the models based on the displacement of the
12 domain walls [33] and experimental results, 5%B, 10%B and 15% B samples are
13 multidomains ($Mr/M_s < 0.1$) for all temperatures. Furthermore, 20%B sample is multidomain
14 for 400 K and pseudo-single domains ($0.1 < Mr/M_s < 0.5$) for 5, 200 and 300 K.

15
16
17
18
19
20
21
22
23
24
25
26
27
28
29
30
31
32
33
34
35
36
37
38
39
40
41
42
43
44
45
46
47
48
49
50
51
52
53
54
55
56
57
58
59
60
61
62
63
64
65

Figure 12 represents the normalized temperature dependence magnetization M–T of the $Fe_{92-x}Nb_8B_x$ ($x=5, 10, 15$ and 20) alloys measured under a magnetic field of 0.05 T in the temperature range of 200–750 K. For lower and higher boron contents, the magnetization curves exhibit different behavior. In fact, the magnetization shows an increase at about 400 K and 670 K for 20%B and 5%B, respectively, that can be attributed to the crystallization of the amorphous phase. On further heating of the 5%B sample beyond 740 K, the decrease of the magnetization to zero can be associated with the ferromagnetic-paramagnetic transition of the α -Fe(Nb, B) solid solution. The effect of the boron content on the composition of the amorphous phase and therefore, the magnetic transition temperature is evidenced by the thermal derivative of the magnetization with respect to the temperature, dM/dT (Fig. 13). The Curie temperature (T_c) increases with increasing B content up to 15%B and then decreases for 20%B. T_c depends on the exchange interaction between the magnetic moments, which in turn depends on the distance between the magnetic atoms. Consequently, T_c depends on the composition of the amorphous structure. Also, the increase of T_c might come from the penetration of the exchange field caused by the NC α -Fe into the residual amorphous matrix [34]. It is well known that B and Nb have different effects on T_c , while B generates strong intergranular magnetic coupling, leading to the increase of T_c , Nb reduces the intergranular coupling thereby decreasing T_c . Thus, the increase of T_c might be related to the B effect while its decrease in the case of 20%B can be due to the presence of Nb atoms in the vicinity

1 of Fe ones. It seems that the overall composition of the residual amorphous phase, rather than
2 the unmixed Fe content alone, appears to determine T_c of the milled powders. Also, the
3 broader peaks in dM/dT curves point out the existence of an inhomogeneous atomic order
4 which results in spreading of the local T_c . This can be due to the hardness and brittleness of
5 boron on the one hand, and its very low solubility in Fe on the other hand. The broadening of
6 the magnetic transition can be linked to the multiphase character of the mechanically alloyed
7 FeNbB system, the presence of impurity phases such as remnant inclusions [6], or the
8 existence of a distribution of T_c in amorphous phases.
9
10
11
12
13
14
15

16 **4. Conclusions**

17 $Fe_{92-x}Nb_8B_x$ ($x = 5, 10, 15$ and 20) powder mixtures have been prepared by MA. The
18 end product consists of an amorphous structure, NC α -Fe and Fe_2B phases. FeB boride is
19 observed for 15 and 20%B samples. The crystallite sizes are in the range of 7–24.3 nm and
20 the volume fraction of the disordered amorphous phase increases with increasing B content,
21 and reaches a maximum value of about 66% for 20%B. As B content increases, H_c increases
22 and M_s decreases. The magnetic hardening is evidenced by the important augmentation of H_c
23 for 20%B sample from 0.014 to 0.0595 T by lowering the temperature from 400 to 5 K,
24 respectively. T_c of the amorphous phase rises with increasing B content up to 15%B and then
25 decreases.
26
27
28
29
30
31
32
33
34
35
36
37

38 **Acknowledgements**

39 This work has been supported by the Algerian Ministère de l'Enseignement Supérieur et de la
40 Recherche Scientifique, the PHC-Maghreb 15 MAG07 program and the Spanish MINECO
41 projects MAT2013-47231-C2-2-P and MAT2016-75967-P.
42
43
44
45
46

47 **References**

- 48 [1] Alleg, S., Ibrir, M., Fenineche, N.E., Azzaza, S., Suñol, J.J., J. Alloys Compds., **494**, 109-
49 115 (2010).
50
51 [2] Bensebaa, N., Loudjani, N., Alleg, S., Dekhil, L., Suñol, J.J., Al Sae, M., Bououdina, M.:
52 J. Magn. Magn. Mater. **349**, 51 (2014).
53
54 [3] Alleg, S. In: Barker, J.M. (ed.) Powder Engineering, Technology and Applications, pp.
55 81–124 Nova Science Publishers, Inc. (2011).
56
57
58
59
60
61
62
63
64
65

- 1
2
3
4
5
6
7
8
9
10
11
12
13
14
15
16
17
18
19
20
21
22
23
24
25
26
27
28
29
30
31
32
33
34
35
36
37
38
39
40
41
42
43
44
45
46
47
48
49
50
51
52
53
54
55
56
57
58
59
60
61
62
63
64
65
- [4] Azzaza, S., Alleg, S., Suñol, J.J.: *J. Therm. Anal. Calo.* **119**, 1037-1046 (2015).
- [5] Bensebaa, N., Alleg, S., Grenèche, J. M., *J. Alloys Compds* **393** 194-203 (2005).
- [6] Ipus, J.J., Blázquez, J.S., Conde, C.F., Borrego, J.M., Franco, V., Lozano-Pérez, S.,
Conde, A., *Intermetallics* **49**, 98-105 (2014).
- [7] Blázquez J.S., Ipus J.J., Conde C.F., Conde, A., *J. Alloys Compds* **615**, S555-S558 (2014).
- [8] Alleg, S., Souilah, S., Younes, A., Bensalem, R., Suñol, J.J., Greneche, J.M.: *J. Alloys
Compds.* **536S**, S394-S397 (2012).
- [9] Varga, L.K., Bakos, E., Koszó, E.K., Zsoldos, E., Kiss, L.F., *J. Magn. Magn. Mater.* **133**,
280 (1994).
- [10] Suñol, J.J., Güella, J.M., Bonastrea, J., Alleg, S., *J. Alloys Compds* **483**, 604-607 (2009).
- [11] Ling-fei, C., Ming-pu, W., Dan, X., Ming-xing, G., Zhou, L., Gen-ying, X.: *Trans. Non
ferrous Met. Soc. China* **16**, 299-303 (2006).
- [12] Ipus, J. J., Blazquez, J.S., Franco, V., Conde, A., Kiss, L. F., *Intermetallics* **18**, 565–568
(2010).
- [13] Blázquez J.S., Ipus J.J., Conde C.F., Conde, A.: *J. Alloys Compds* **615**, S555-S558
(2014).
- [14] Li, W., Yang, Y. Z., Xu, J., Xie, C. X., *J Supercond Nov Magn* **30**, 1877 (2017).
- [15] Stoica, M., Hajlaoui, K., Das, J., Eckert, J., Yavari, A.R., *Rev. Adv. Mater. Sci* **18**, 61-65
(2008).
- [16] Varga, L.K., Bakos, E., Koszó, E.K., Zsoldos, E., Kiss, L.F., *J. Magn. Magn. Mater.* **133**,
280 (1994).
- [17] Balogh, J., Kemény, T., Vincze, I., Budjosó, L., Tóth, L., Vincze, G., J., *Appl. Phys.* **77**,
(1995) 4997.
- [18] Alleg, S., Hamouda, A., Bensalem, R., Suñol, J.J., Grenèche, J.M., Azzaza, S.: *Mater.
Chem. Phys.* **122**, 35-40 (2010).
- [19] Calca, A., Radlinski, A. P.: *Mater. Sci. Eng.* **134**, 1350–1353 (1991).
- [20] Imafuku, M., Sato, S., Koshiba, H., Matsubara, E., Inoue, A., *Scripta mater.* **44**, 2369-
2372 (2001).
- [21] Životský, O., Postava, K., Kraus, L., Jirásková, Y., Juraszek, J., Teillet, J., Barčová, K.,
Švec, P., Janičkovič, D., Pištora, J., *J. Magn. Magn. Mater.* **320** 1535–1540 (2008).
- [22] Škorvánek, I., Kováč, J., Marcin, J., Duhaj, P., Gerling, R.: *J. Magn. Magn. Mater.* **203**,
226-228 (1999).
- [23] Suñol, J.J., González, A., Saurina, J., Escoda, L., Bruna, P.: *Mater. Sci. Engin. A*

375–377, 874-880 (2004).

- 1
2 [24] Torrens-serra, J., Bruna, P., Rodriguez-Viejo, J., Roth, S., and Clavaguera-Mora, M. T.,
3 Intermetallics **18**, 773-780 (2010).
4
5 [25] Lutterotti, L.: MAUD version 2.55, <http://maud.radiographema.com/>
6
7 [26] Rietveld, H.M., J. Appl. Cryst. **2**, 65-71 (1969).
8
9 [27] Blasquez, J.S., Franco, V., Conde, C.F., Conde, A., Intermetallics **15**, 1351-1360 (2007).
10
11 [28] Takeuchi, A., Inoue, A., Mater. Trans. **46**, 2817-2829 (2005).
12
13 [29] Hasegawa, R., Ray, R., J. Appl. Phys. **49** 4174 (1978).
14
15 [30] Azzaza, S., PhD Thesis University of Annaba, Algeria (2009).
16
17 [31] Massalski, T.B.: Binary alloy phase diagrams, 2nd Edn. ASM International, Materials
18 Park, Ohio (1990)
19
20 [32] Rico, M.M., Grenèche, J.M., Alcazar, G.A.P., J. Alloys Compd. **398**, 26-32 (2005).
21
22 [33] Fallot, M. : Masson et Cie (1935).
23
24 [34] Hernando, A., Amils, X., Nogués, J., Suriñach, S., Baró, M.D., Ibarra, M.R.: Phys. Rev.
25 B **58**, R11 864 (1998).
26
27
28
29
30
31
32
33
34
35
36
37
38
39
40
41
42
43
44
45
46
47
48
49
50
51
52
53
54
55
56
57
58
59
60
61
62
63
64
65

1
2 **Figure captions**

3 **Figure 1:** SEM micrographs of $\text{Fe}_{92-x}\text{Nb}_8\text{B}_x$ powders. The insets show the EDX analysis.

4
5 **Figure 2:** XRD patterns of $\text{Fe}_{92-x}\text{Nb}_8\text{B}_x$ powders.

6
7 **Figure 3:** Rietveld refinement of the XRD patterns of $\text{Fe}_{92-x}\text{Nb}_8\text{B}_x$ powders.

8
9 **Figure 4:** B content dependence of the crystallite size of Fe_2B .

10
11 **Figure 5:** Evolution of the phases relative proportions as a function of B content.

12
13 **Figure 6:** Lattice parameters evolution against B content of bcc α -Fe and amorphous phase.

14
15 **Figure 7:** Lattice parameters evolution of Fe_2B boride phase as a function of B content.

16
17 **Figure 8:** Hysteresis loops of the $\text{Fe}_{92-x}\text{Nb}_8\text{B}_x$ ($x = 5, 10, 15$ and 20) powders , taken for
18 different temperatures. The inset shows the enlargement of the central part and the
19 first magnetization curve .
20

21
22 **Figure 9:** Variation of coercivity, H_c , and amorphous phase proportion as a function of B
23 content.
24

25
26 **Figure 10:** Evolution of saturation magnetization, M_s , and amorphous phase proportion vs. B
27 content.
28

29 **Figure 11:** Changes of squarness ratio, M_r/M_s , against B content.

30
31 **Figure 12:** Temperature dependence magnetization M - T of the $\text{Fe}_{92-x}\text{Nb}_8\text{B}_x$ compounds
32 measured under a magnetic field of 0.05 T.
33

34
35 **Figure 13:** dM/dT variation as a function of temperature.
36
37
38
39
40
41
42
43
44
45
46
47
48
49
50
51
52
53
54
55
56
57
58
59
60
61
62
63
64
65

1
2
3 **Table captions**

4 **Table 1:** EDX analysis of the $\text{Fe}_{92-x}\text{Nb}_8\text{B}_x$ powders.
5

6 **Table 2:** Lattice parameters (a, b and c), crystallite size, $\langle L \rangle$, microstrains, $\langle \sigma^2 \rangle^{1/2}$ and
7 relative proportions of the ball milled $\text{Fe}_{92-x}\text{Nb}_8\text{B}_x$ (x=5, 10, 15 and 20) powders for 50 h.
8
9

10
11
12
13
14
15
16
17
18
19
20
21
22
23
24
25
26
27
28
29
30
31
32
33
34
35
36
37
38
39
40
41
42
43
44
45
46
47
48
49
50
51
52
53
54
55
56
57
58
59
60
61
62
63
64
65

Table 1

Sample	Element		
	Fe (wt.%)	Nb (wt. %)	B (wt. %)
5% B	76.27	1.71	22.92
10% B	62.93	2.46	34.61
15% B	94.13	4.38	1.49
20% B	72.7	2.64	24.66

Table 2

Sample	Phase	a (nm) $\pm 10^{-4}$	Δa (%)	b (nm) $\pm 10^{-4}$	Δb (%)	c (nm) $\pm 10^{-4}$	Δc (%)	$\langle L \rangle$ (nm) ± 2	$\langle \sigma^2 \rangle^{1/2}$ $\pm 10^{-3}$	Proportions (%)
5% B	α -Fe	0.2867	0.04	-----	-----	-----	-----	07.45	0.62	16.0
	Fe (B)	0.2899	1.15	-----	-----	-----	-----	12.35	1.32	24.0
	Fe ₂ B	0.5162	1.02	-----	-----	0.4205	-1.03	08.32	0.39	12.4
	Amorphous	0.2897	-----	-----	-----	-----	-----	10	0.001	47.6
10% B	α -Fe	0.2867	0.04	-----	-----	-----	-----	19.60	0.39	06.4
	Fe ₂ B	0.5169	1.15	-----	-----	0.4198	-1.20	08.24	0.26	38.9
	Amorphous	0.2914	-----	-----	-----	-----	-----	10	0.001	54.7
15% B	α -Fe	0.2868	0.07	-----	-----	-----	-----	23.11	0.28	29.3
	Fe ₂ B	0.5173	1.23	-----	-----	0.4194	-1.29	08.10	0.98	09.6
	FeB	0.4080	0.66	0.5709	3.89	0.3040	3.19	10.11	0.24	04.9
	Amorphous	0.2927	-----	-----	-----	-----	-----	10	0.001	56.2
20% B	α -Fe	0.2867	0.04	-----	-----	-----	-----	24.28	0.32	06.9
	Fe ₂ B	0.5208	1.20	-----	-----	0.4175	-1.74	08.84	0.17	09.7
	FeB	0.4137	2.07	0.5577	1.49	0.2972	0.88	10.69	0.43	17.4
	Amorphous	0.2963	-----	-----	-----	-----	-----	10	0.001	66

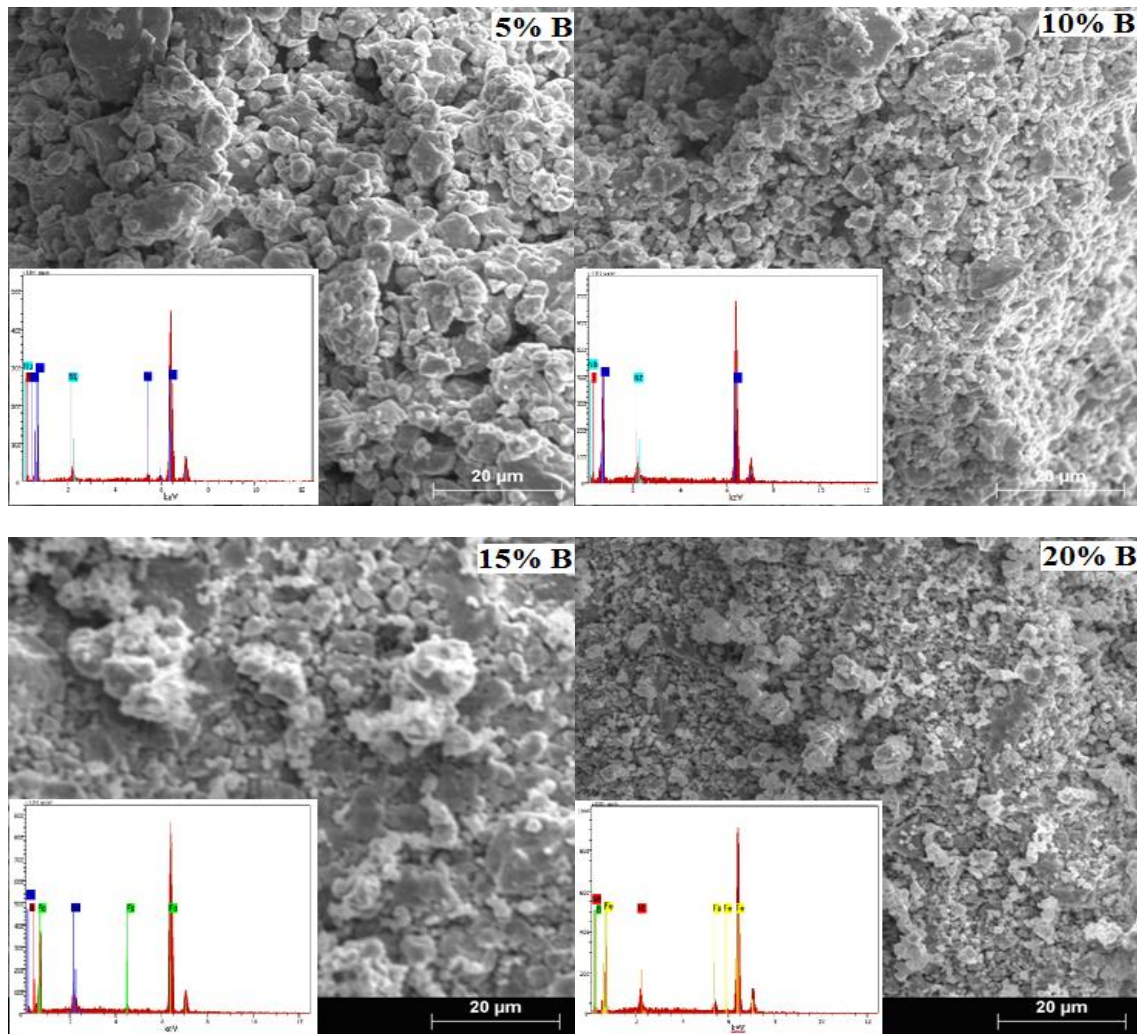


Figure 1

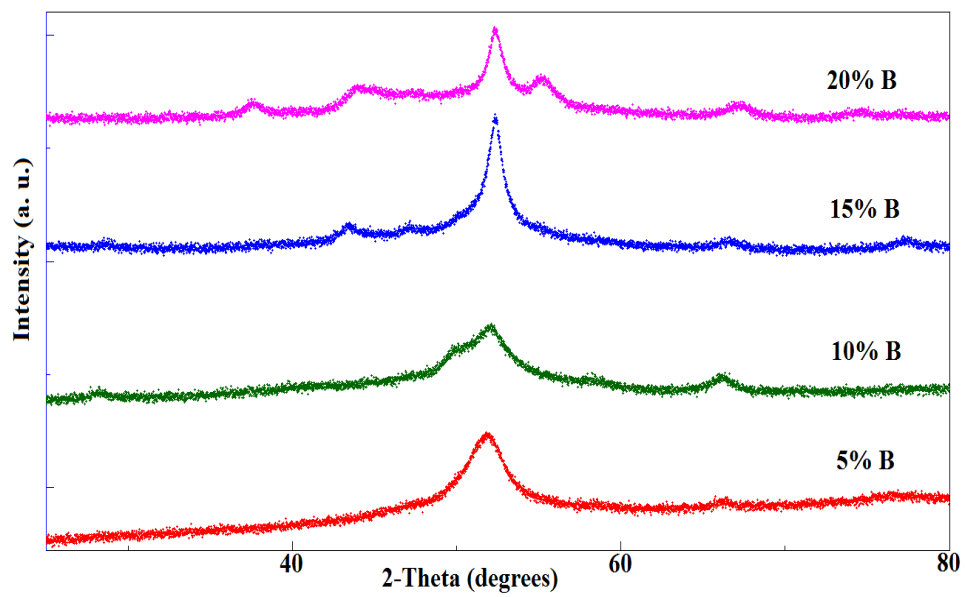


Figure 2

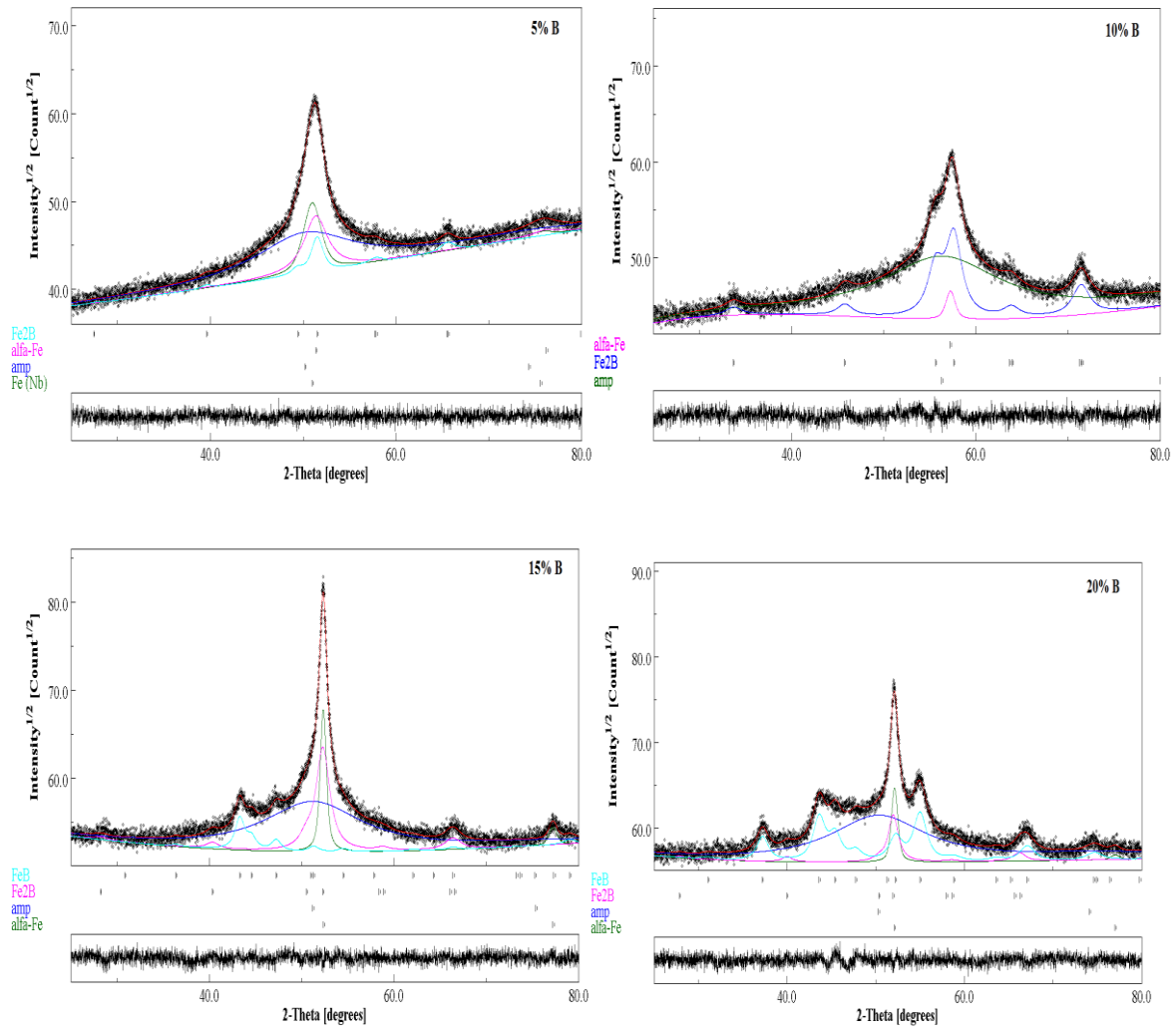


Figure 3

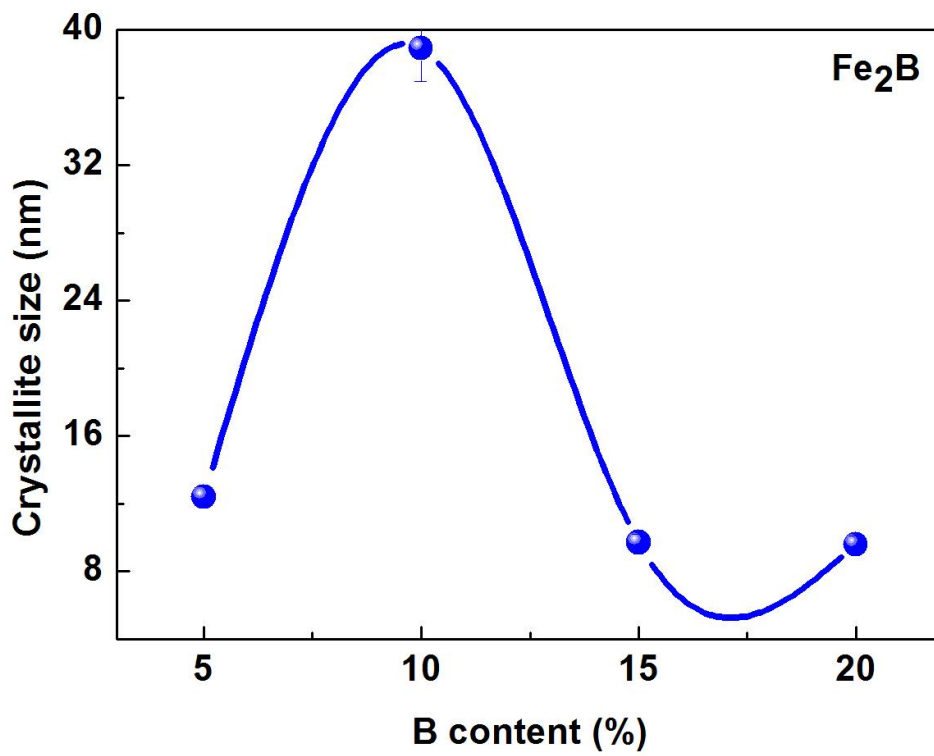


Figure 4

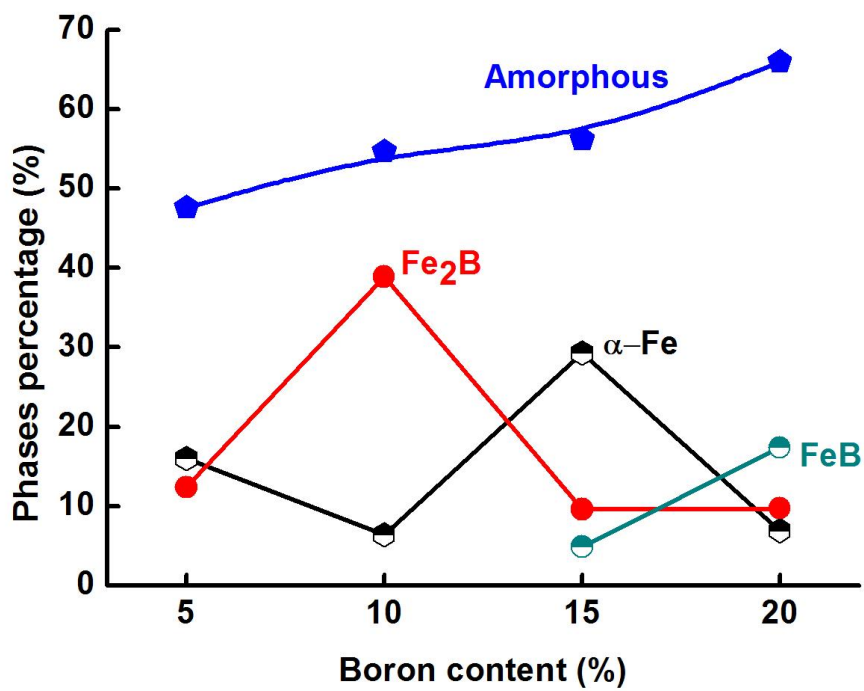


Figure 5

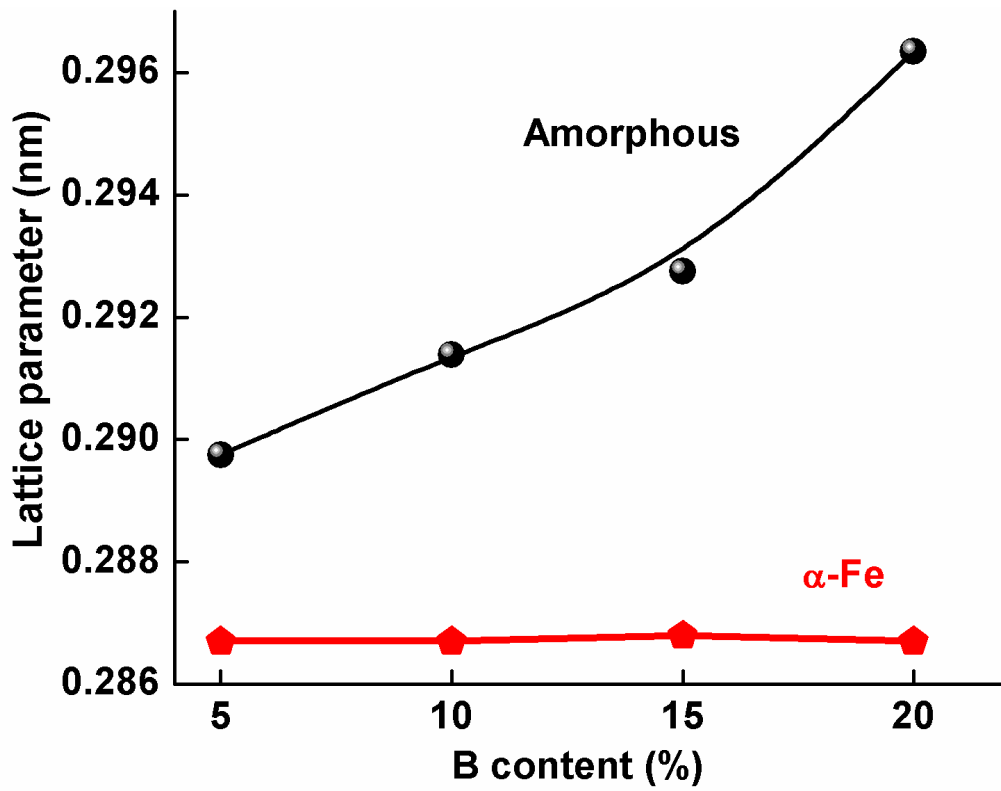


Figure 6

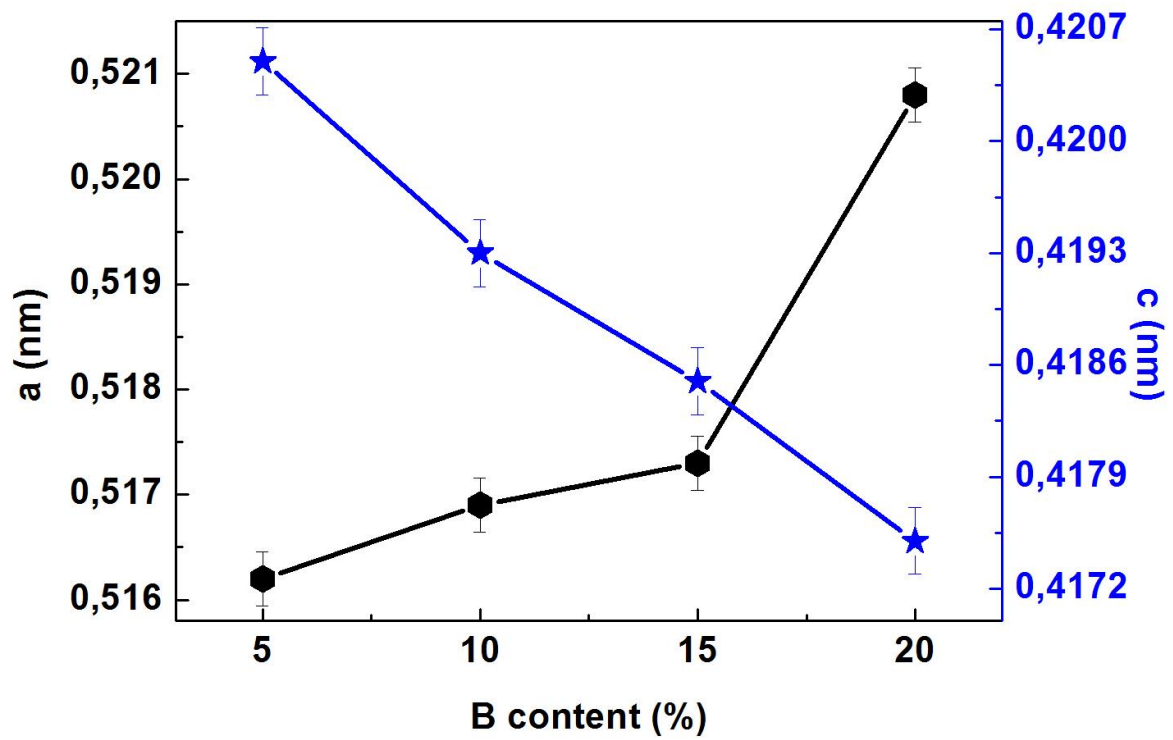
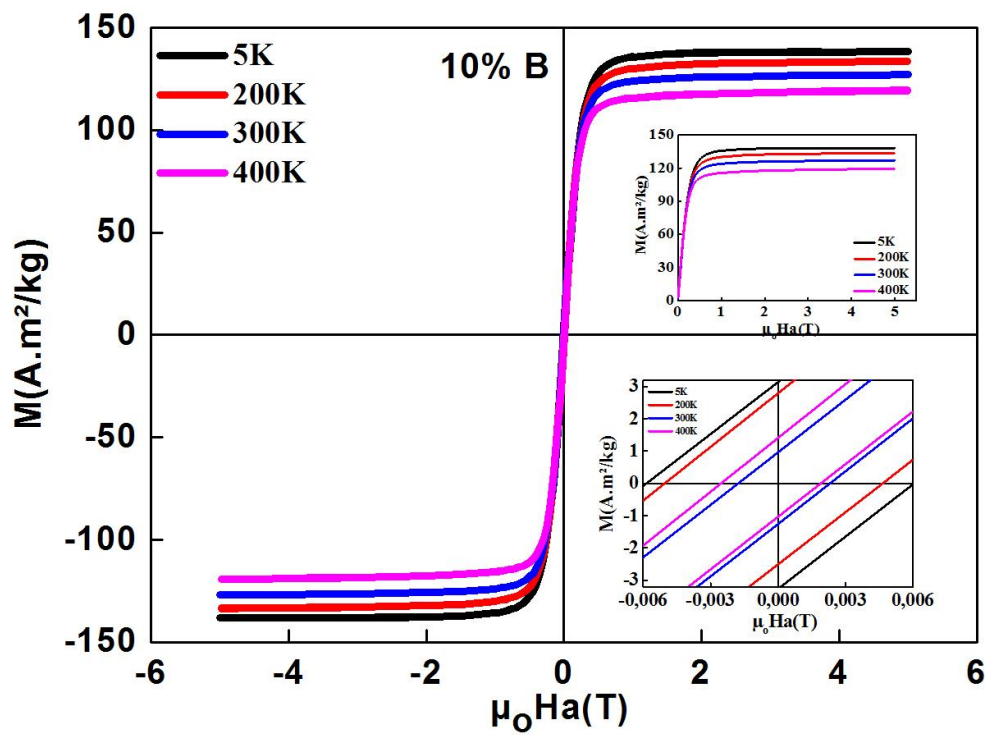
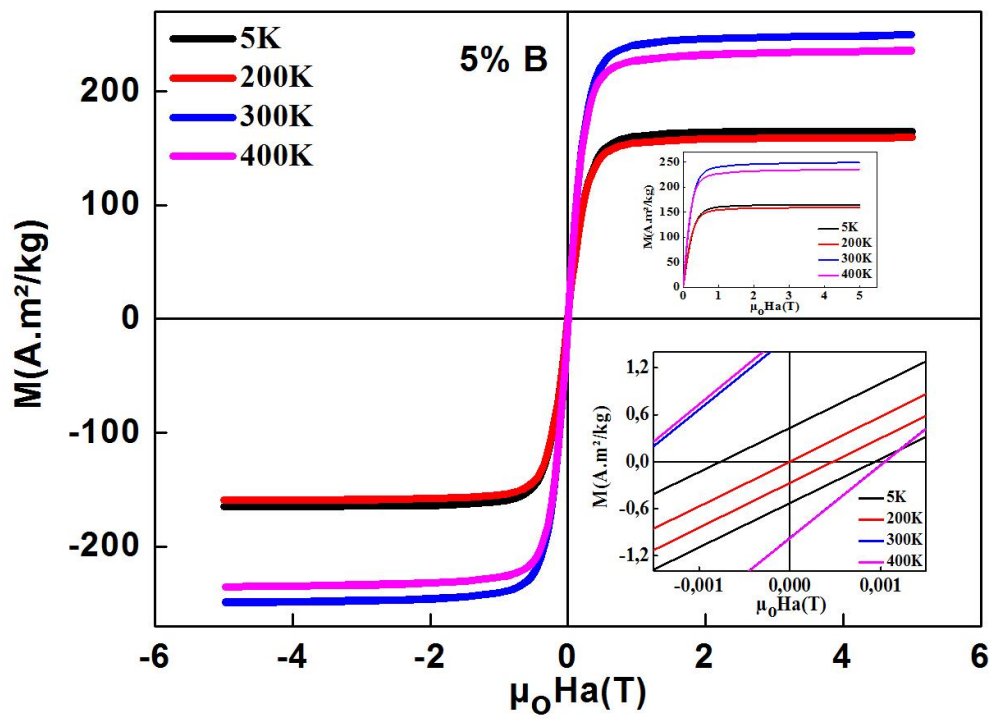


Figure 7



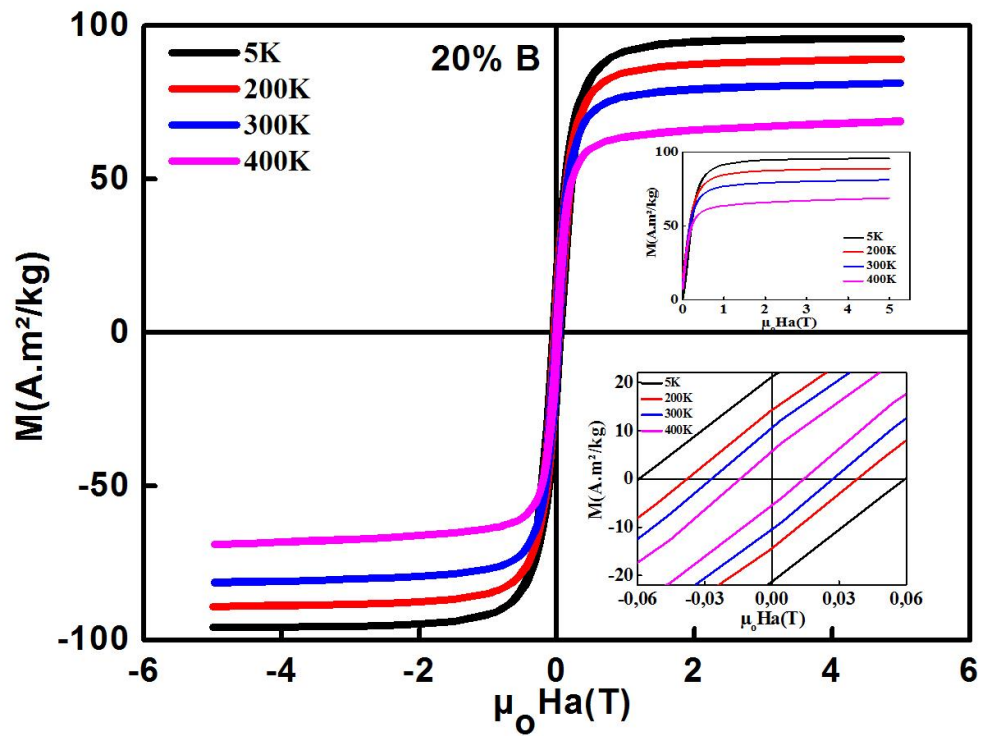
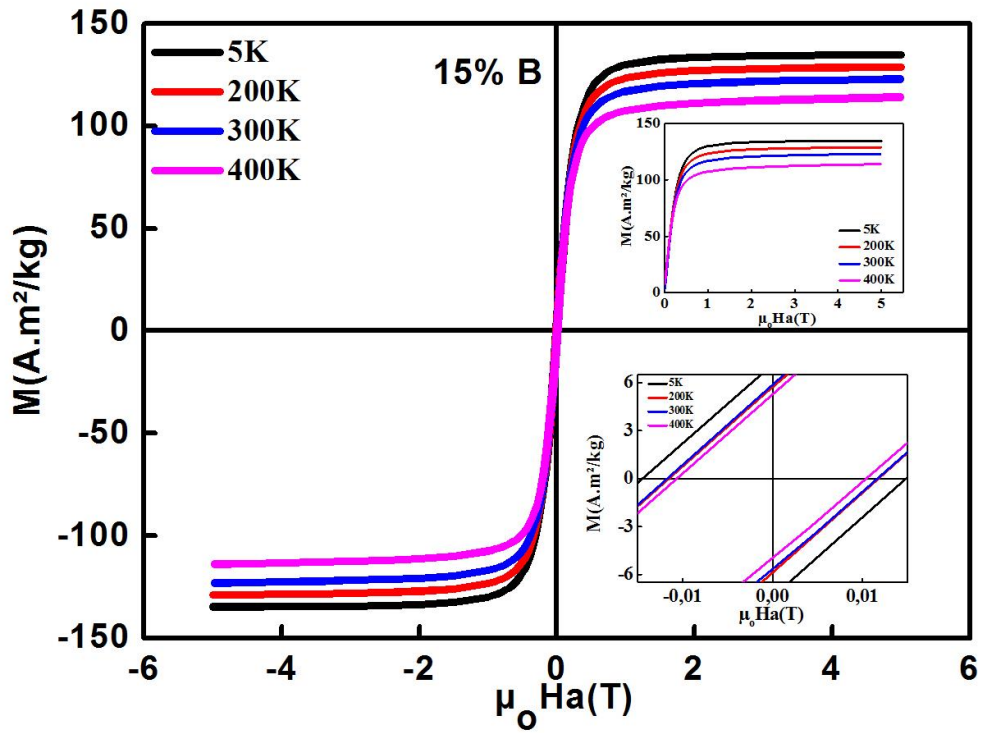


Figure 8

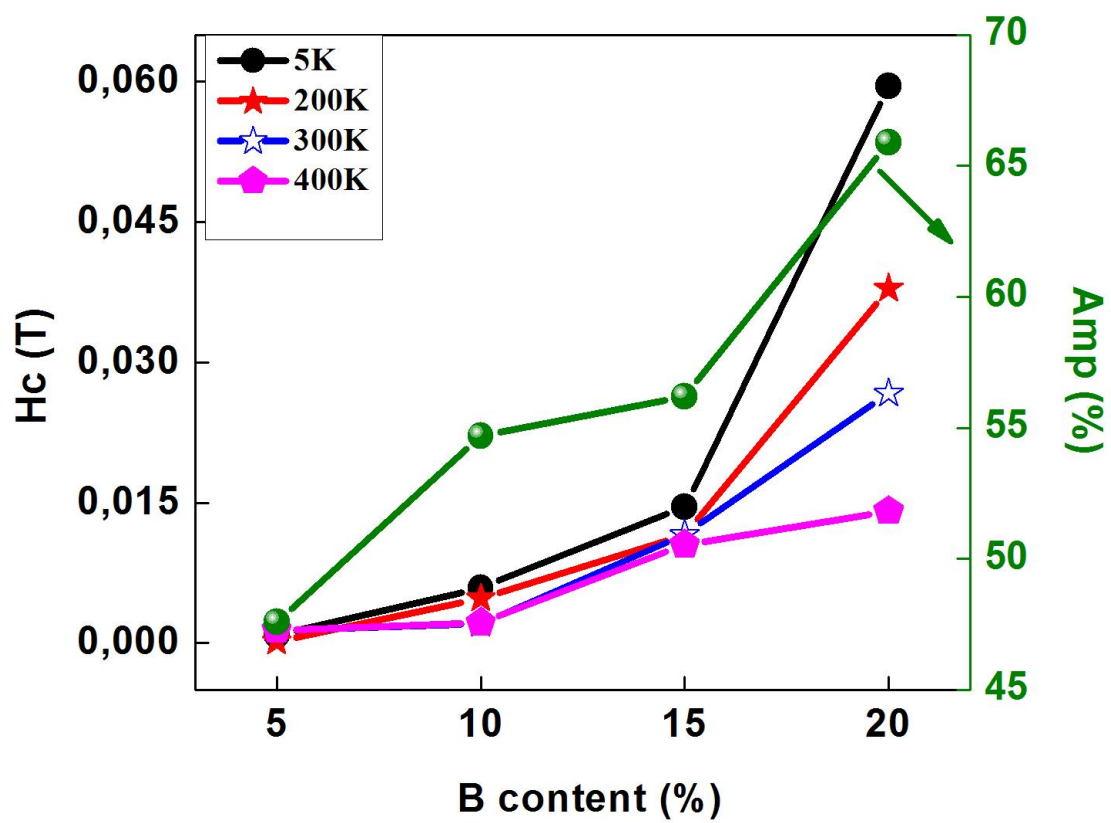


Figure 9

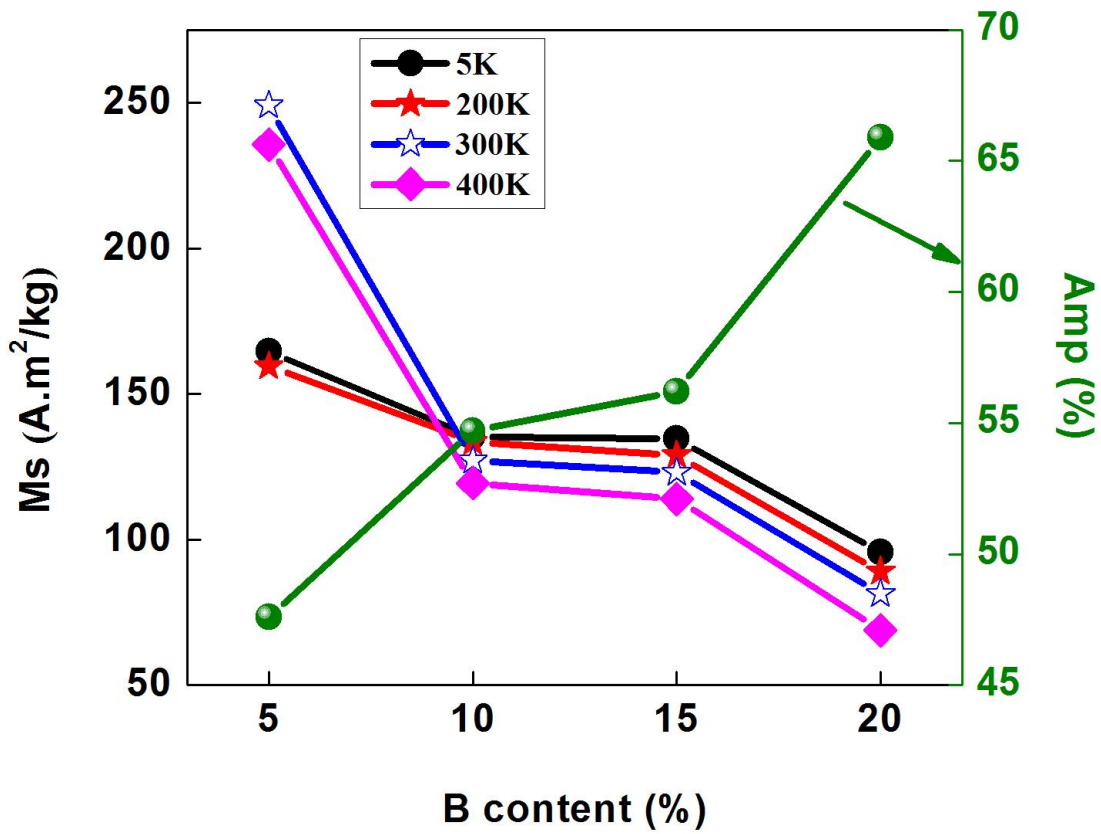


Figure 10

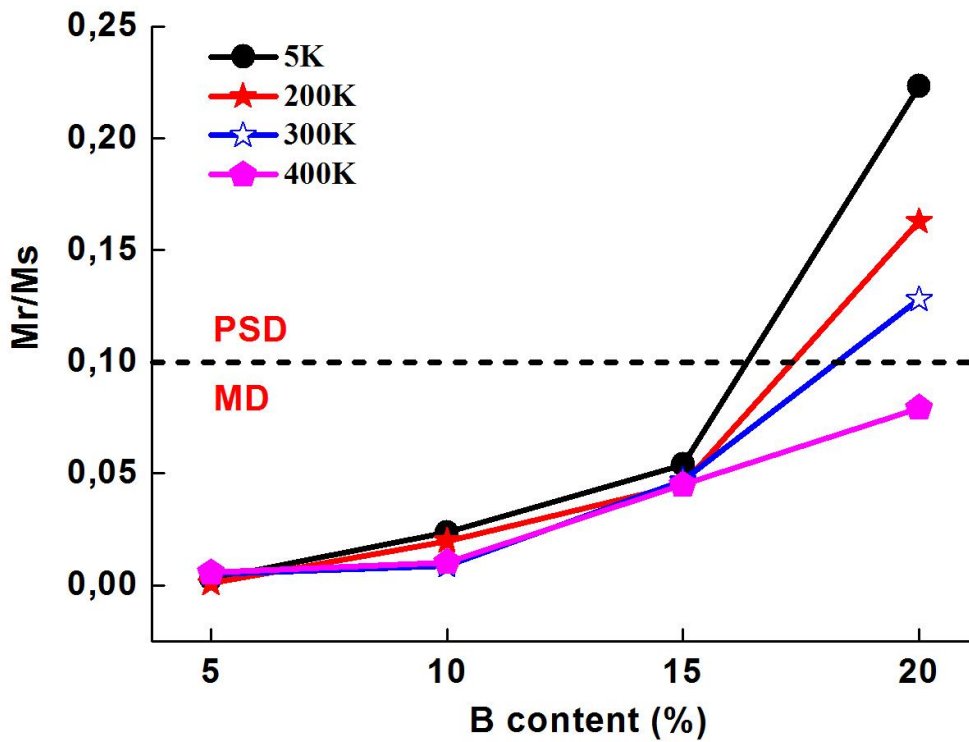


Figure 11

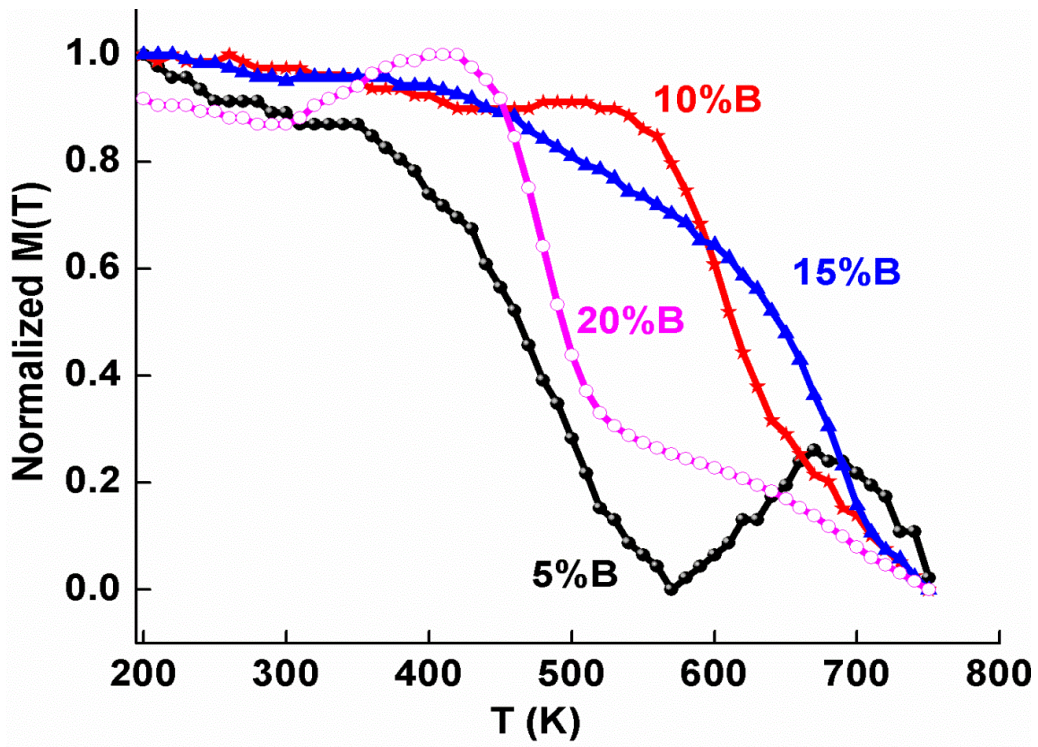


Figure 12

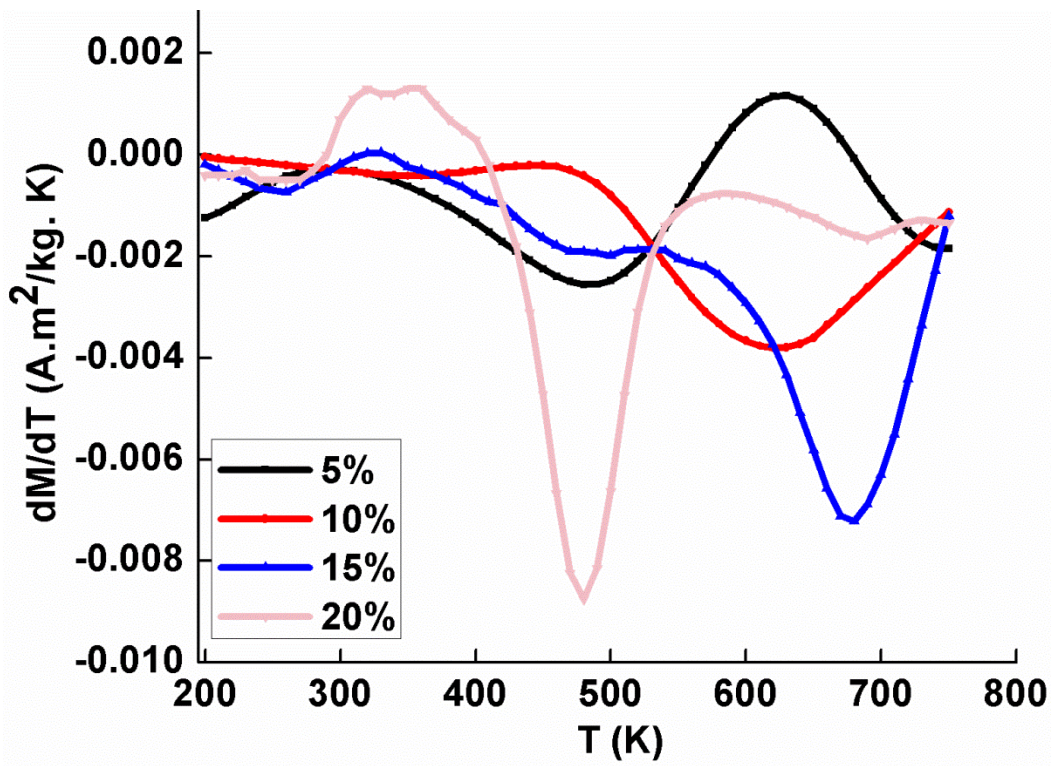


Figure 13